

Enhanced boiling heat transfer using conducting-insulating microcavity surfaces in an electric field: A lattice Boltzmann study

Fanming Cai, Zhaomiao Liu*, Nan Zheng, Yan Pang*

Faculty of materials and manufacturing, Beijing University of Technology, Beijing, China

* Corresponding author. E-mail address: lzm@bjut.edu.cn and pangyan@bjut.edu.cn

Abstract

In electronic chip cooling, constrained by the field trap effect on the microcavity surfaces under the action of an electric field, the boiling heat transfer performance cannot realize significant improvement. This study found through lattice Boltzmann simulations that using conducting-insulating microcavity surfaces in an electric field removes the field trap effect, increasing the critical heat flux by more than 200%. Bubble behavior and heat transfer mechanisms on heating surfaces were further explored. The results show that a large electrical force can be generated at the junction of the conducting and insulating surfaces under the action of the electric field, which drives the bubbles in the cavity to departure quickly from the heating surface and avoids the formation of a vapor film at a medium superheat. In the high superheat, increasing the electric field intensity can cause the contact line to produce a pinning phenomenon, which inhibits the development of capillary waves in the cavity and facilitates the formation of multiple continuously open vapor-liquid separation paths on the heating surface, resulting in a significant enhancement of the boiling heat transfer performance.

Keywords: Boiling, Electric field, Lattice Boltzmann method, Numerical simulation

1. Introduction

Boiling heat transfer utilizes the latent heat of vapor-liquid phase change and bubble-induced micro-convection, which allows heat transfer coefficients to be increased by orders of magnitude compared with traditional single-phase convection and thus is widely used in the cooling process of a variety of microelectronic devices characterized by high thermal loads^[1-2]. However, when the heat transfer power exceeds the limit (i.e., critical heat flux [CHF]), the heating surface is rapidly covered by a vapor film that causes the surface temperature to surge, which may lead to severe damage to the equipment. Therefore, improving the CHF of the heating surface is important for developing the electronics industry.

Existing schemes for enhancing critical heat flux can be categorized into passive and active techniques. Typical strategies for passive techniques are to utilize surface microstructures (e.g., microcavities, micropillars, and porous media) to decrease the bubble departure size^[3,4], increase the bubble departure frequency^[5,6], and enhance capillary wicking^[7,8] to improve the CHF. However, under microgravity conditions, due to the disappearance of buoyancy, achieving the effective removal of bubbles only by surface microstructure is difficult, which is likely to cause vapor film formation on the heating surface and thus reduce the CHF^[9]. Introducing an external force field instead of the buoyancy effect is particularly important in this situation. Electric field as an active control scheme has the advantages of low power consumption, non-contact and high stability, which can effectively improve boiling heat transfer performance^[10]. Previous studies have shown that electrical forces can avoid bubbles merging at high superheat levels by squeezing the vapor-liquid

interface, which delays CHF occurrence^[11,12]. Under the influence of an electric field, the boiling process can produce bubble sizes close to those of normal gravity conditions, even in a microgravity environment^[13].

To combine the respective advantages of electric fields and micro-structured surfaces, researchers in recent years have focused on the effect of the coupled behavior of both on the performance of boiling heat transfer. Garivalis et al.^[14] have experimentally demonstrated that electric fields and micro-structured surfaces can enhance boiling heat transfer synergistically. Even more significant enhancement of CHF can be achieved in a microgravity environment. However, Quan^[15] and Liu et al.^[16] suggested that coupling electric field and micro-structured surfaces would inhibit the boiling heat transfer. The above differences may come from the different surface structure parameters. When the height (depth) of the micropillar (microcavity) used is large, the region of high electric field intensity formed at its top will inhibit the growth and departure of bubbles at the root (i.e., the field trap effect), thus deteriorating the boiling performance. Although some researchers set additional hydrophobic spots^[17] or microcavities^[18] on the top of the microstructures to mitigate the field trap effect, generating bubbles in the root still hinders the heat transfer when the superheat is large enough. Therefore, the field trap effect is not entirely removed. Designing novel heating surfaces is urgently needed to realize the optimal heat transfer effect of the combination of electric field and micro-structured surface.

This study proposes a conducting-insulating microcavity surface that can eliminate the field trap effect through lattice Boltzmann simulations. The boiling heat transfer mechanism of conducting-insulating microcavity surfaces under the influence of an electric field is further revealed by exploring the thermodynamic relationship between the bubble behavior and the thermal response of the heater bottom. The study's results can provide theoretical and applied technical guidance for the structural design of novel heating surfaces.

2. Model description

This study designs a conducting-insulating surface and establishes a numerical model for vapor-liquid two-phase flow and phase change heat transfer, as shown in Fig. 1, to eliminate the field trap effect. The bottom of the computational domain is a heating surface with microcavities of height H_0 , width W_0 , and depth D_0 . The central regions at the bottom and top of the microcavities have a conducting block of width W_e , and the rest of the surfaces are insulated. When the height from the top of the microcavity is greater than H_e , the system maintains a constant high potential U , and the potential of the conducting block is zero (electric field intensity $E_0=U/H_e$). The thermal response of the solid-liquid interface needs to be obtained by numerical calculations and is not predetermined.

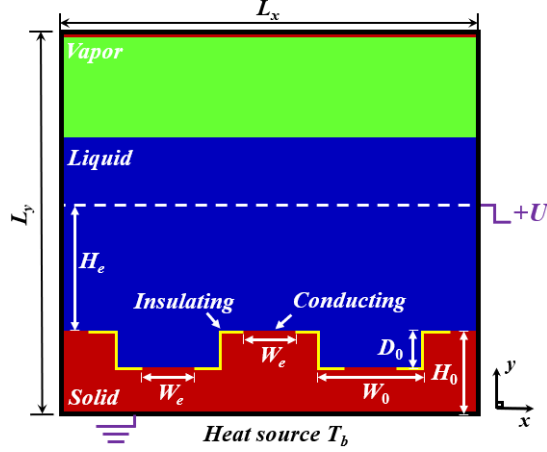


Fig. 1 Schematic of the conducting-insulating microcavity surfaces under the action of an electric field.

The governing equation for obtaining the vapor-liquid two-phase flow based on the multi-relaxation pseudo-potential lattice Boltzmann method can be formulated as follows^[19]:

$$f_\alpha(\mathbf{x} + \mathbf{e}_\alpha \Delta t, t + \Delta t) = f_\alpha(\mathbf{x}, t) - (\mathbf{M}^{-1} \mathbf{\Lambda} \mathbf{M})_{\alpha\beta} [f_\alpha(\mathbf{x}, t) - f_\alpha^{eq}(\mathbf{x}, t)] + \Delta t F'_\alpha(\mathbf{x}, t),$$

$$\rho(\mathbf{x}, t) = \sum_{\alpha} f_\alpha(\mathbf{x}, t),$$

$$\rho \mathbf{u}(\mathbf{x}, t) = \sum_{\alpha} f_\alpha(\mathbf{x}, t) \mathbf{e}_\alpha + \frac{\mathbf{F}(\mathbf{x}, t) \Delta t}{2},$$
(1)

where f_α is the distribution function related to density and \mathbf{x} and t denote the spatial location and time of the distribution function, respectively. $\Delta t = 1$ is the time step, and \mathbf{e}_α (where α is the orbital direction of the distribution function) is the lattice speed of the D2Q9 model. \mathbf{M} is an orthogonal transformation matrix, and $\mathbf{\Lambda}$ is a diagonal matrix^[19]. \mathbf{F} denotes the body force on the fluid, including the inter-particle interaction force \mathbf{F}_{int} , the adhesion force between liquid/vapor and solid \mathbf{F}_{ads} , and the gravitational force \mathbf{F}_g .

$$\mathbf{F}_{int} = -G\psi(\mathbf{x}) \sum_{\alpha=1}^8 w_\alpha \psi(\mathbf{x} + \mathbf{e}_\alpha \Delta t) \mathbf{e}_\alpha,$$

$$\mathbf{F}_{ads} = -G_w \psi(\mathbf{x}) \sum_{\alpha=1}^8 w_\alpha s(\mathbf{x} + \mathbf{e}_\alpha \Delta t) \mathbf{e}_\alpha,$$

$$\mathbf{F}_g = (\rho - \rho_{ave}) \mathbf{g},$$
(2)

where w_α are the weighting coefficients ($w_0=4/3$, $w_{1-4}=1/3$ and $w_{5-8}=1/12$). ρ_{ave} is the average density of the whole fluid domain, and $\mathbf{g}=(0, -g)$ is the gravitational acceleration. The desired contact angle can be obtained by changing the fluid-solid interaction strength G_s . $s(\mathbf{x})$ is the indicator function equal to 1 when \mathbf{x} is a solid node and 0 when \mathbf{x} is a fluid node.

$$\psi(\mathbf{x}) = \sqrt{\frac{2(p_{EOS} - \rho c_s^2)}{G}},$$

$$p_{EOS} = \frac{\rho RT}{1 - b\rho} - \frac{a\rho^2 \alpha(T)}{1 + 2b\rho - b^2 \rho^2},$$
(3)

$$\alpha(T) = [1 + (0.37464 + 1.54226\omega - 0.26992\omega^2)(1 - \sqrt{T/T_c})]^2$$

where p_{EOS} represents Peng-Robinson (P-R) equation of state. ω is the central factor, and R is the gas constant. For the vapor-liquid phase change process of water, this study sets $a=3/49$, $b=2/21$,

$R=1$ and $\omega=0.344$, corresponding to the critical temperature $T_c=0.1094$.

According to the local balance law for entropy, the energy equation considering the vapor-liquid phase change can be expressed as follows^[20]:

$$\frac{\partial T}{\partial t} = -\mathbf{u}\nabla T + \frac{1}{\rho c_v} \nabla \cdot (\lambda \nabla T) - \frac{T}{\rho c_v} \left(\frac{\partial p_{EOS}}{\partial T} \right)_\rho \nabla \cdot \mathbf{u}, \quad (4)$$

where T , c_v , and λ denote temperature, heat capacity, and thermal conductivity, respectively. The fourth-order Runge-Kutta scheme is adopted for time discretization. The other gradient terms are discretized numerically using the finite volume method.

For numerical modeling of electrohydrodynamic, previous studies usually assume that the vapor-liquid two phases are perfect dielectrics, i.e., no free-moving charge is found at the interface^[16]. Therefore, the governing equation of the electric field can be expressed as follows:

$$\nabla \cdot (\varepsilon \mathbf{E}) = 0, \quad (5)$$

where ε denotes the dielectric constant and \mathbf{E} is the electric field intensity. When the electric field vectors are irrotational, the electric field intensity \mathbf{E} is related to the potential gradient (i.e., $\mathbf{E}=-\nabla U$). Equation (5) can be rewritten as follows:

$$\nabla \cdot (\varepsilon \nabla U) = 0, \quad (6)$$

The potential distribution in the system can be obtained by solving Eq. (6) by the finite difference method. For a perfect dielectric with incompressibility, the electrical force \mathbf{F}_e at the vapor-liquid interface is obtained from the following equation:

$$\mathbf{F}_e = -\frac{1}{2} E^2 \nabla \varepsilon \quad (7)$$

The electrical force \mathbf{F}_e needs to be introduced into Eq. (1) as one of the external forces to change the vapor-liquid two-phase flow.

The simulation grid size was $L_x \times L_y = 400 \text{ l.u.} \times 600 \text{ l.u.}$ (l.u. means lattice units). Periodic conditions are imposed on the left and right boundaries of the computational domain, and constant temperature boundaries are used at the bottom and top. The initial fluid domain with $y < 0.70L_y$ is saturated liquid, and $y > 0.70L_y$ is saturated vapor. The saturation temperature is $T_{sat}=0.86T_c$. The equilibrium densities of the liquid and vapor were obtained by Maxwell's construction as $\rho_l=6.5$ and $\rho_v=0.38$, respectively. The static contact angle is $\theta=30.0^\circ$, and the gravitational acceleration is $\mathbf{g} = (0, -0.00003)$. The thermal conductivity ratio between solid and liquid is $\lambda_s/\lambda_l=50$. The specific heat at a constant volume is $c_{V,s}=c_{V,l}=c_{V,v}=6.0$. The solid density is $\rho_s=1.5\rho_l$. The dynamic viscosity ratio and thermal conductivity ratio of the liquid to the vapor are $\mu_l/\mu_v=17$ and $\lambda_l/\lambda_v=17$, respectively. The structural parameters of the conducting-insulating microcavity surface were as follows: $H_0=50$ l.u., $W_0=100$ l.u., $D_0=10$ l.u., $W_e=50$ l.u. The latent heat of the vapor-liquid phase change was determined to be $h_{lv}=0.58$ from the theoretical analysis^[21]. The vapor-liquid surface tension coefficient obtained via Laplace's law test was $\gamma=0.086$. If not specified, the electric field intensity $E_0=0.08$ remains constant. Referring to the study by Feng et al.^[22], the dielectric constants of vapor and liquid are $\varepsilon_v=1.0$ and $\varepsilon_l=2.24$, respectively. The parameters used in this study are all in lattice units.

The characteristic length l_0 and time t_0 are typical dimensions to describe the boiling process.

$$l_0 = \sqrt{\frac{\sigma}{(\rho_l - \rho_v)g}}, \quad t_0 = \sqrt{l_0 / g}, \quad (8)$$

The boiling heat transfer performance can be assessed from the dimensionless heat flux $Q''(x,t)$ at the bottom of the heater and the surface superheat Ja :

$$Q''(x,t) = \frac{\int_{t_a}^{t_b} Q'(t) dt}{t_b - t_a}, \quad Ja = \frac{c_p (T_w - T_{sat})}{h_{lv}}, \quad (9)$$

where t_a to t_b is a longer time interval. T_w is the space- and time-averaged wall temperature over the heating surface. $Q'(x,t)$ is the space-averaged dimensionless heat flux:

$$Q'(x,t) = -\frac{\lambda_s \cdot l_0}{\mu_l h_{lv}} \cdot \frac{\int_0^{L_x} \nabla_y T|_{x,0} dx}{L_x}, \quad (10)$$

The temperature gradient ($\nabla_y T|_{x,0}$) at the bottom of the heater can be obtained in a second-order differential format.

3. Model validation

3.1 Validation of the boiling model

The boiling curve on a smooth surface is simulated and compared with the classical correlation equation to verify the correctness of the numerical model of phase change heat transfer developed in this study. As the superheat Ja increases, the heating surface sequentially experiences natural convection, the onset of nucleate boiling (ONB), and the CHF, as shown in Fig. 2. The boiling curve of the smooth surface obtained from LB simulations is compared with the Rohsenow's correlation equation^[23]:

$$Ja = C_{sf} \left(\frac{Q}{\mu_l h_{lv}} \sqrt{\frac{\sigma}{g(\rho_l - \rho_v)}} \right)^{0.33} \left(\frac{C_{p,l} \mu_l}{\lambda_l} \right)^{1.7}, \quad (11)$$

where C_{sf} is a fitting coefficient in the range of 0.006 to 0.0130 and related to the physical properties of the heating surface. The red solid line in Fig. 2 indicates the fitting result with $C_{sf} = 0.0068$. The heat flux obtained from the simulation is consistent with the Rohsenow's correlation equation. Zuber proposed an empirical correlation formula for CHF^[24]:

$$Q_{CHF} = K \rho_v h_{fg} \left(\frac{\sigma(\rho_l - \rho_v)g}{\rho_v^2} \right)^{-0.5}, \quad (12)$$

where K is the fitting coefficient between 0.12 and 0.16^[25]. Q_{CHF} can be further expressed in the dimensionless form $Q''_{CHF} = Q_{CHF} l_0 / \mu_l h_{lv}$. The $Q''_{CHF} = 0.133$ obtained from the numerical simulation is closer to the predicted value 0.155 ($K=0.12$), which verifies the correctness of the model.

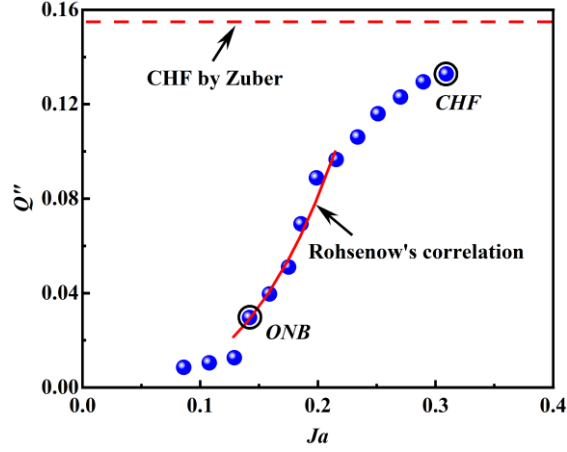


Fig. 2 Boiling curves for smooth surfaces.

3.2 Deformation of droplets in the electric field

The deformation of a static droplet under the action of an electric field is simulated to verify the correctness of the electric field-multiphase phase flow model. A circular droplet of radius $R_d=251.u.$ is placed statically in a square cavity with a computational domain of $4R_d \times 4R_d$. A high potential is maintained at the top of the square cavity, and the bottom of the square cavity is grounded. The deformation of the droplet under the electric field is defined as $D=(L-B)/(L+B)$, where L and B are the lengths of the long and short axes, respectively, as shown in the inset of Fig. 3. The effect of the dielectric constant ratio $\varepsilon_r(=\varepsilon_l/\varepsilon_v)$ on the droplet deformation D at different electrical capillary numbers $Ca_E(=\varepsilon_r R_d E^2/\gamma)$ is given in Fig. 3. Allan and Mason^[26] provided an analytical solution for the droplet deformation D :

$$D = \frac{9}{16} Ca_E \frac{(\varepsilon_r - 1)^2}{(\varepsilon_r + 2)^2}, \quad (13)$$

The droplet deformation D increases with the dielectric constant ratio ε_r . The numerical model developed in this study agrees well with the theoretical values when the dielectric constant ratio is 1.5 to 2.5.

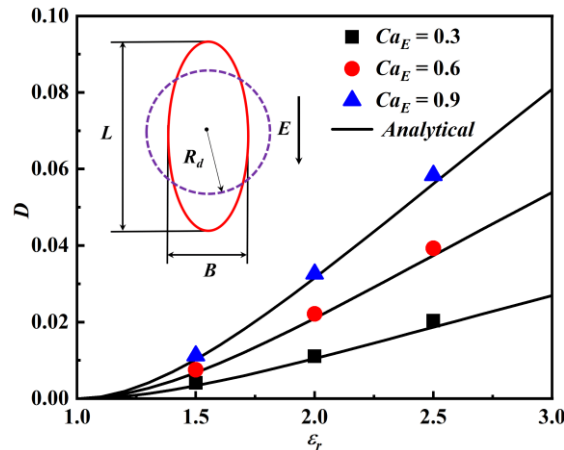


Fig. 3 Effect of electric field on droplet deformation.

4. Results and discussion

This section gives the boiling curves for the smooth surface (SS), the microcavity surface (MC), the uniformly conducting microcavity surface (MC-UCS), and the conducting-insulating

microcavity surface (MC-CIS). The heat transfer mechanism of the heating surface under the action of electric field (EF) was revealed by analyzing the bubble behavior and the thermal response of the heater bottom. Finally, the effects of different electric field intensities on CHF were explored, and a new predictive correlation equation was established.

4.1 Boiling curves

The boiling curves for the four heating surfaces (SS, MC, MC-UCS, and MC-CIS) are shown in Fig. 4. In the natural convection stage with low superheat ($Ja < 0.12$), thermal accumulation occurs at the bottom of the microcavity when the thermal conductivity of the liquid is significantly lower than the solid, which negatively affects heat transfer compared with smooth surfaces^[27]. The microcavity structure provides potential nucleation sites on the heating surface, so ONB can appear at lower superheat (Fig. 4(b)). At medium superheat ($0.15 < Ja < 0.20$), the heat flux of MC-UCS is higher than that of SS but lower than that of MC, which is consistent with the experimental results of Quan et al^[15]. Notably, the MC-CIS proposed in this study improves the suppression of the boiling heat transfer from the microcavity surface by the electric field at medium superheat. As the superheat continuously increases ($Ja > 0.20$), the heating surface enters the fully developed nucleate boiling stage. Eventually, many bubbles aggregated and merged on the heating surface, which hindered the reflux of the bulk liquid to make CHF occur.

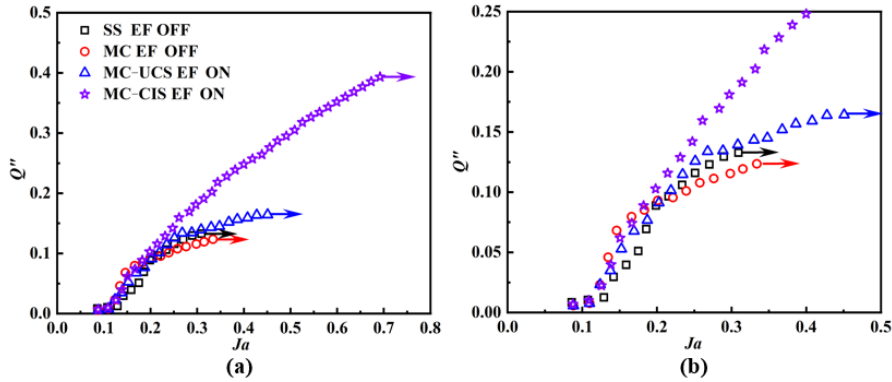


Fig. 4 Boiling curves for different surfaces. (a) $0 < Ja < 0.8$; (b) $0 < Ja < 0.5$.

Unlike the previous experimental studies^[28,29], the heat transfer performance of microcavity surfaces is weaker than that of smooth surfaces at high superheat ($Ja > 0.20$). At $Ja = 0.30$, the heat fluxes of MC and SS are 0.115 and 0.133, respectively, as shown in Fig. 4. The LB simulation used a higher saturation temperature ($T_{sat} = 0.86T_c$), resulting in a lower two-phase flow density ratio. Therefore, the bubbles generated at the bottom of the microcavity are larger and tend to merge to form a vapor film, thus increasing the thermal resistance of the MC. When the electric field was activated, the boiling curves of MC-UCS and MC-CIS shifted to the left side of MC and SS, indicating that the electric field improved the boiling heat transfer performance of the heating surface at high superheat. The CHF of the four heating surfaces are given in Fig. 5. The CHF of SS, MC, MC-UCS, and MC-CIS are 0.133, 0.123, 0.164, and 0.393, respectively. Given the field trap effect, the CHF of the MC-UCS is only 33.0% higher than that of the MC. When the field-trapping effect is removed for MC-CIS, the CHF increases by 219.5% over MC.

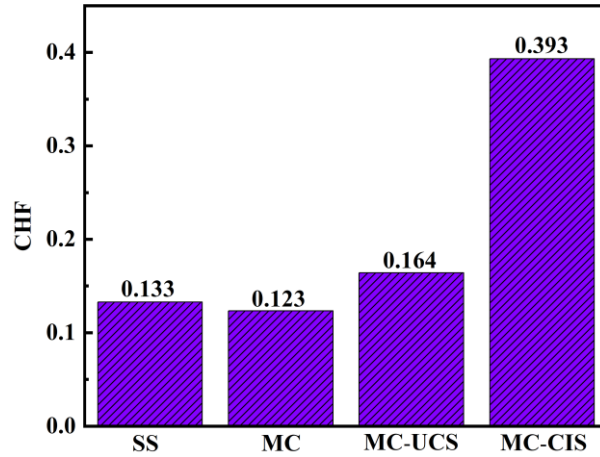


Fig. 5 CHF on different surfaces.

4.2 Bubble behaviors and heat transfer mechanism

The iso-potential lines and electric field intensity distributions of MC-UCS and MC-CIS are given in Fig. 6 (only the electric field distribution was calculated numerically) to understand the mechanism of synergistic enhancement of boiling heat transfer by the electric field and microcavity surfaces. For MC-UCS, the heating surface maintains a constant electric potential, which causes significant distortion and aggregation of the iso-potential lines at the corners of the top of the microcavity, which locally generates a large electric field intensity (i.e., $\mathbf{E} = -\nabla U$). The phenomenon is similar to the numerical results of Liu^[16] and Li et al^[17]. According to Eq. (7), the electrical force positively correlates with the electric field intensity, which means that the bubbles generated in the microcavity are continuously suppressed on the heating surface. For the MC-CIS proposed in this study, since the corners of the microcavity are electrically insulated, the potential gradient in the direction perpendicular to the wall is zero, which produces a low electric field intensity locally. Moreover, iso-potential line changes dramatically at the junction of the conducting and insulating surfaces, resulting in a significant increase in the electric field intensity compared with the MC-UCS.

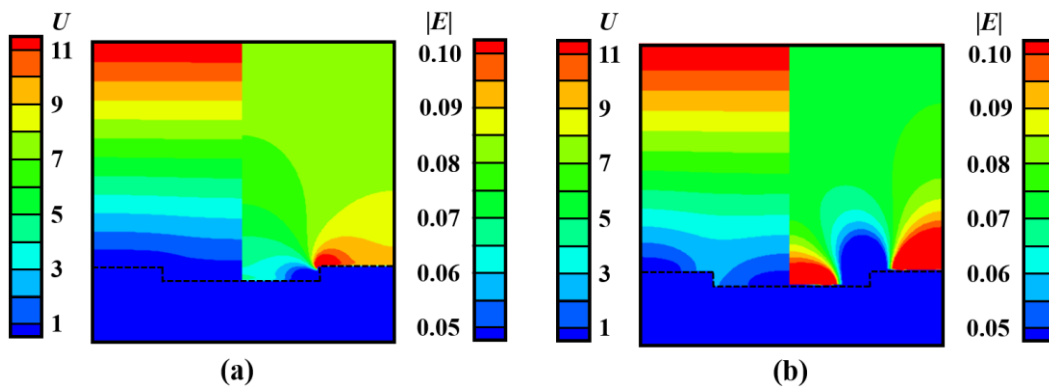


Fig. 6 Distribution of iso-potential line U and electric field intensity $|E|$. (a) MC-UCS. (b) MC-CIS. The black dashed line indicates the solid-liquid interface.

The reorganization of the spatial electric field will affect the characteristics of the electrical force distribution at the vapor-liquid interface, which will change the processes of bubble nucleation, growth, and departure. Figure 7 shows the boiling behavior of the four surfaces for $T_b = 0.102T_c$ ($Ja \approx 0.15$) (time intervals are located within the first three boiling cycles of the heating surfaces).

The bubble is the blue region, and the solid heater is the red region. The comparison of the boiling behavior in Figs. 7(a) and 7(b) reveals that the microcavity corners provide additional vaporization cores, resulting in a significant increase in boiling heat transfer performance at medium superheat. When the electric field is activated, the high electric field intensity present at the top surface of the microcavity accelerates bubble departure, but bubble growth inside the microcavity is inhibited by the field trap effect. At $t^*=35.3$, the bubble necks at the corners are just forming, and the bubble sizes in the center region of the microcavity are small(Fig. 7(c)). Corresponding to Fig. 7(b), the first boiling cycle in the microcavity has been completed (i.e., the bubble neck is broken). The bubble size is larger in the center region of the microcavity. Prolonged attachment of bubbles to the bottom of the microcavity causes localized hot spots on the heating surface, negatively affecting the boiling heat transfer performance. In general, the top of the microcavity is farther away from the high-temperature heat source, resulting in less bubble than inside the microcavity. Thus, the field trap effect occurring within the uniformly conducting microcavity significantly hinders the enhancement of the overall boiling performance of the heating surface, resulting in the boiling curve of the MC-UCS being on the right side of the MC at medium superheat, as shown in Fig. 4(b).

For MC-CIS, the high electric field intensity is generated inside and at the top of the microcavity. The electric field intensities are weaker at the corner structures, so the field trap effect is eliminated (Fig. 6). From Fig. 7(d), the bubble generation period is reduced when the field trap effect disappears. The boiling performance is enhanced compared with MC-UCS. At $t^*=35.3$, the bubbles in the center region of the microcavity are about to detach from the heating surface, and the bubbles at the corners have already detached. However, the numerical results show that the boiling performance of MC-CIS is still slightly weaker than that of MC at medium superheat (Fig. 4(b)). For MC, small bubbles tend to merge into large bubbles, which cause strong convection when they depart from the heating surface, which facilitates the rapid cooling of the heating surface by the low-temperature bulk liquid (Fig. 7(b), $t^*=58.9$). For MC-CIS, the electrical force in the microcavity hinders the lateral movement of the bubbles, and the bubbles do not merge with each other, making the convection effect weak (Fig. 7(d), $t^*=58.9$). In summary, the boiling heat transfer performance $MC > MC-CIS > MC-UCS > SS$ at medium superheat.

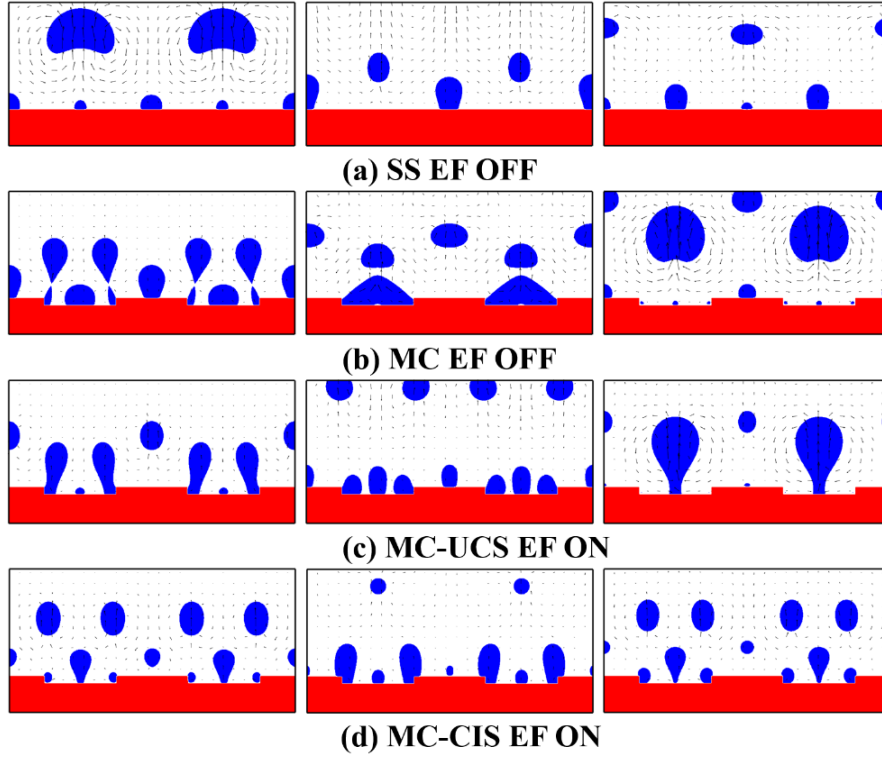


Fig. 7 Boiling behavior of different surfaces at $T_b = 0.102 T_c$ ($Ja \approx 0.15$) (from left to right: $t^* = 35.3, 47.1$ and 58.9 . time $t^* = t/t_0$). Black arrows indicate the velocity vectors.

As the superheat increases, bubbles depart from the heating surface, leaving residual vapors behind. This phenomenon is more pronounced on heating surfaces with microcavities. Figure 8 shows the boiling behavior of different surfaces at $T_b=0.120T_c$ ($Ja\approx 0.30$). For SS, the three-phase contact line of the bubbles retracts under surface tension, which facilitates the continuous replenishment of the bulk liquid to the heating surface. For MC, the three-phase contact line of the bubble was always pinned at the cavity mouth. The vapor trapped in the cavity increased the thermal resistance of the heating surface and hindered the bulk liquid reflux. Thus, the MC exhibited poorer heat transfer performance and lower CHF than the SS (Fig. 4(b)).

Theoretical studies have shown that the electric field can increase CHF by decreasing the Taylor wavelength^[30]. A similar phenomenon was observed in LB simulations. For MC, the vapor film inside the microcavity was always stable over the heating surface during the complete boiling cycle (Fig. 8(b)). For MC-UCS, the interface breaks up into three isolated small bubbles at the position of the thinnest vapor film when the large bubbles detach (Fig. 8(c), $t^*=35.3\sim 47.1$). The electrical force and electric field intensity distributions of the MC-UCS at $t^*=35.3$ are given in Fig. 9(a) to explain the breakup mechanism of the vapor film further. Given that the dielectric constant of the liquid is greater than that of the vapor, an electrical force is found at the interface of the two phases pointing toward the bubbles' interior (the dielectric constant gradient $\nabla\epsilon$ determines the direction of the electrical force). Equation (6) shows that the magnitude of the electric potential is related to the dielectric constant, which leads to the vapor-liquid interface morphology to change the spatial electric field distribution. The iso-potential line changes dramatically at the location of the thinnest vapor film within the microcavity^[31], which locally generates a larger electric field intensity and increases the squeezing of the vapor film by the electrical force, thus promoting interfacial breakup, as shown in Fig. 9(a). Therefore, MC-UCS at high superheat may improve

boiling performance by promoting bubble breakup near the heating surface.

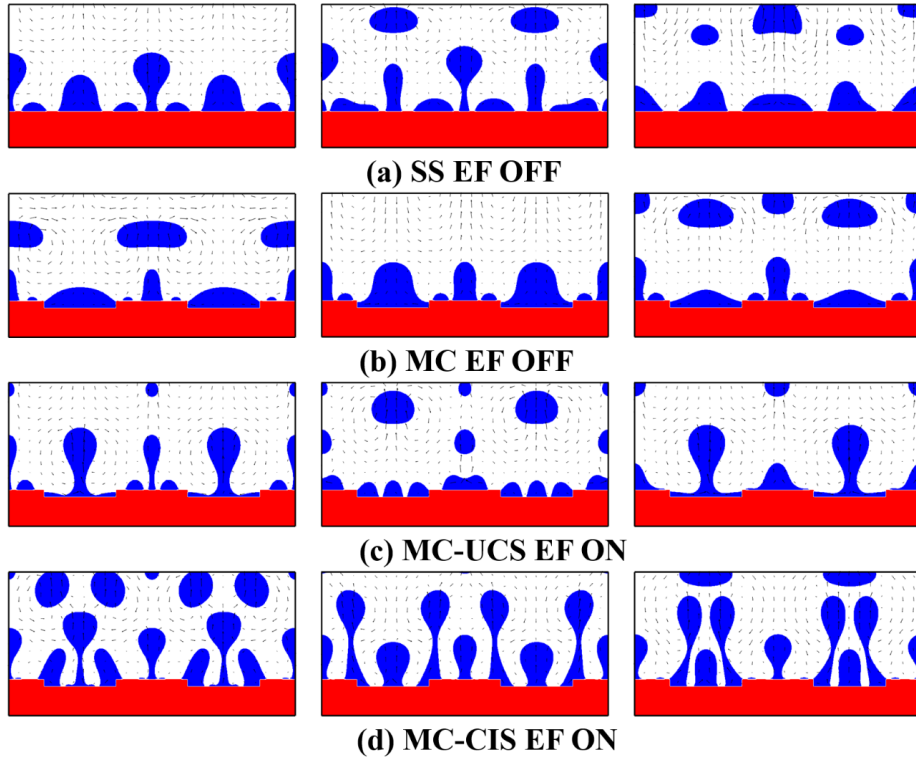


Fig. 8 Boiling behavior of different surfaces at $T_b = 0.120 T_c$ ($Ja \approx 0.30$) (from left to right: $t^* = 35.3, 47.1$ and 58.9).

No vapor film appears in the microcavity at $T_b=0.120T_c$ for the MC-CIS, as shown in Fig. 8(d). At the junction of the conducting and insulating surfaces, the electrical force increased significantly (Fig. 9(b)), which caused the pinning of the contact line, thus hindering the merging of the bubbles in the cavity. This phenomenon provides multiple continuously open vapor-liquid separation paths on the heating surface, which effectively enhances the convective heat transfer in the cavity and delays the occurrence of CHF.

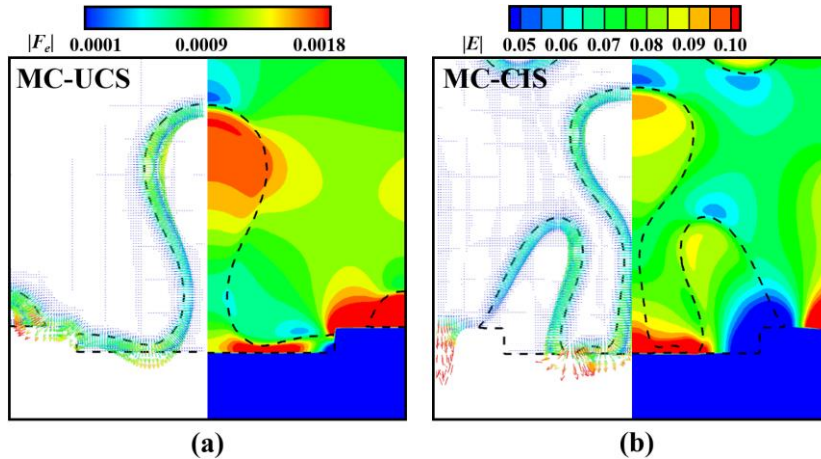


Fig. 9 Distributions of electrical force $|F_e|$ and electrical field intensity $|E|$ during bubble departure ($T_b=0.120T_c$, $t^*=35.3$). (a) MC-UCS. (b) MC-CIS.

SS and MC reached CHF further increasing the superheat of the heating surface. The vapor-liquid interfacial morphology (white dashed line) and temperature field of MC-UCS and MC-CIS at $T_b=0.134T_c$ are given in Fig. 10. For MC-UCS, the larger vapor pressure inside the microcavity at sufficiently high superheat offsets the electrical force, allowing the perturbation of the interface

to be suppressed. In this case, the vapor layer stably covers the microcavity and increases the local thermal resistance. For MC-CIS, the contact lines are still pinned at the junction of the conducting and insulating surfaces. As the vapor is produced in large quantities, the bubbles, which are squeezed by the electrical force into a rod shape, depart after merging at a location away from the heating surface. Figure 11 shows the heater bottom time-averaged temperatures of the MC-UCS and MC-CIS at $T_b=0.134T_c$ ($t^*=35.3\sim 58.9$). At the bottom of the microcavity ($50\text{l.u.}<x<150\text{l.u.}$ and $250\text{l.u.}<x<350\text{l.u.}$), the highest and lowest temperatures were observed for MC-UCS and MC-CIS, respectively, indicating that the proposed novel heating surface improves the heat transfer in the cavity. At the top surface of the microcavity ($150\text{l.u.}<x<250\text{l.u.}$), the non-uniform electrical force generated by the MC-CIS promotes bubble departure and facilitates the re-wetting of the wall by the bulk liquid, as shown in Fig. 10(b). As a result, a localized low-temperature region appears on the top surface of the microcavity (Fig. 11). For MC-UCS, the electrical force tends to act uniformly on the vapor-liquid interface, which is detrimental to the bubble departure and increases the localized temperature (Fig. 11). In conclusion, the boiling heat transfer performance MC-CIS > MC-UCS > SS > MC at high superheat (Fig. 4).

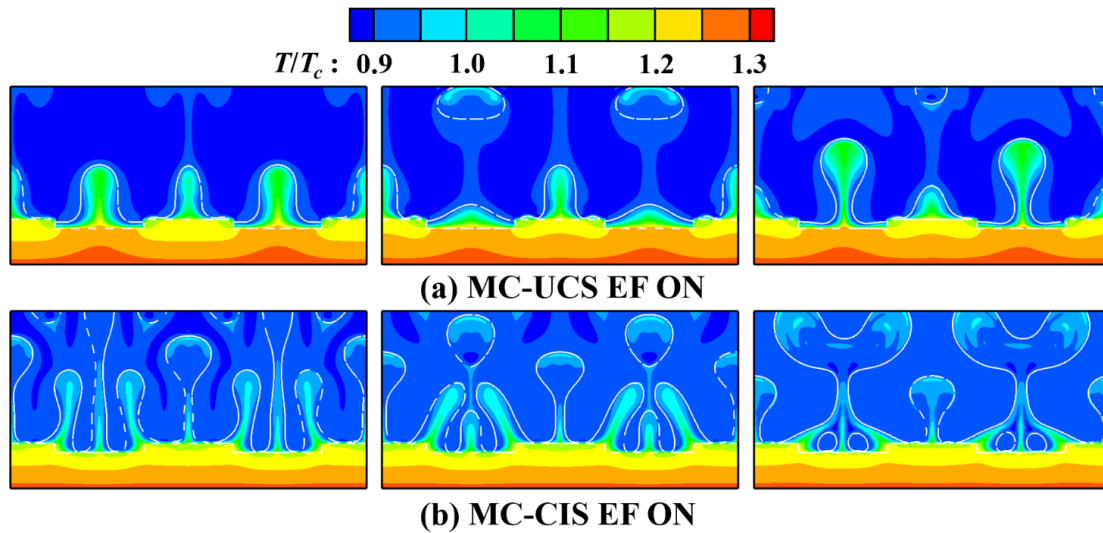


Fig. 10 Temperature fields in the computational domain at $T_b = 0.134 T_c$ (from left to right: $t^* = 35.3, 47.1$ and 58.9). (a) MC-UCS. (b) MC-CIS.

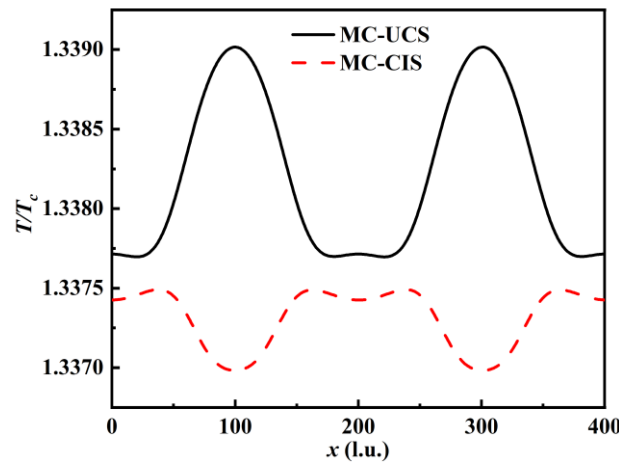


Fig. 11 Time-averaged temperatures at the bottom of the heaters of MC-UCS and MC-CIS at $T_b = 0.134 T_c$ ($t^* = 35.3$ to 58.9).

4.3 Effect of electric field intensity on boiling curves with MC-CIS

Figure 12 shows the boiling curves with MC-CIS at different electric field intensities. Gong et al.^[32] found a second transition point in the boiling curve (the slope of the boiling curve starts to decrease) as the superheat increases, which comes from the formation of permanent dry spots. The figure shows that different electric field intensities have less effect on the boiling curve before the appearance of the second transition point. However, larger electric field intensities can delay the superheat required for the appearance of the second transition point. The reason is that the electrical force acting on the contact line promotes the departure of bubbles, thus preventing the dry spot from persistently adhering to the heating surface (Fig. 9(b)). Particularly, a sufficiently large electric field intensity ($E_0 = 0.080$) can cause the second transition point to disappear.

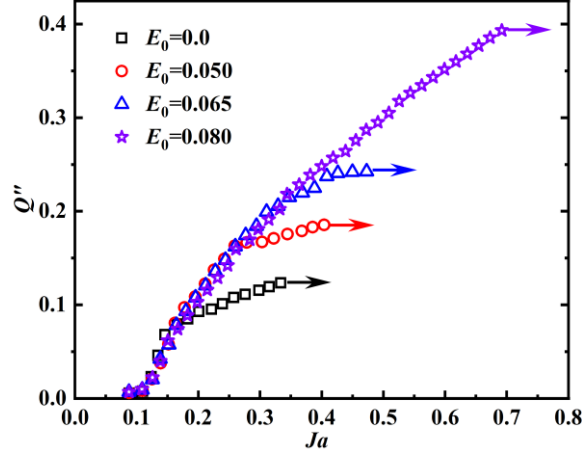


Fig. 12 Boiling curves of MC-CIS at different electric field intensities.

CHF is the main factor limiting the improvement of the cooling performance of electronic chips, so the prediction of CHF is especially important. The CHF correlation for a smooth surface in a uniform electric field was proposed by Johnson et al.^[30]:

$$r_{CHF} = Q''_{CHF,E} / Q''_{CHF,0} = \sqrt{\frac{El^* + \sqrt{El^* + 3}}{\sqrt{3}}}, \quad (14)$$

$$El^* = \frac{\varepsilon_l(\varepsilon_l - \varepsilon_v)^2 E_0^2}{\varepsilon_v(\varepsilon_l + \varepsilon_v)\sqrt{(\rho_l - \rho_v)\sigma g}},$$

where r_{CHF} is the enhancement ratio of CHF under a uniform electric field and $Q''_{CHF,0}$ is the CHF at $E_0=0$. For conducting-insulating microcavity surfaces, the iso-potential lines are reorganized, which changes the spatial electric field intensity distribution. Based on the analysis in Section 4.2, lower electric field intensity exists at corners and does not negatively affect boiling heat transfer. An electric field intensity much higher than that of the smooth surface SS is generated at the junction of the conducting and insulating surfaces. Therefore, the effective electric field intensity E_e can be regarded as enhanced compared to SS. The effective electric field intensity E_e can be decomposed into two parts. The first part is the electric field intensity E_0 on a smooth surface. The second part is the additional electric field intensity ψE_0 caused by local iso-potential line changes. The corrected electric field intensity is as follows:

$$E_e = E_0(1 + \psi), \quad (15)$$

where ψ is the fitting coefficient related to the structure of the heating surface. Therefore, the modified El^* can be expressed as follows:

$$El^* = \frac{(1+\psi)^2 \varepsilon_l (\varepsilon_l - \varepsilon_v)^2 E_0^2}{\varepsilon_v (\varepsilon_l + \varepsilon_v) \sqrt{(\rho_l - \rho_v) \sigma g}}, \quad (16)$$

Figure 13 gives the effect of the square of the electric field intensity E_0^2 on the enhancement ratio r_{CHF} and compares the Johnson correlation and modified results. When $E_0^2 < 0.005$, r_{CHF} increases linearly with E_0^2 . Numerical results are gradually larger than predicted values when $E_0^2 > 0.005$. Given that the Johnson correlation equation does not consider the effect of microstructure on the electric field enhancement, predicted values become lower. For the modified correlation equation proposed in this study, the predicted values are in good agreement with the numerical results at $E_0^2 < 0.005$ (ψ taken as 0.64).

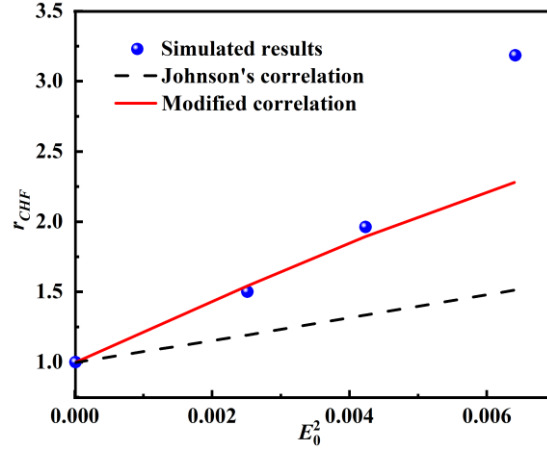


Fig. 13 Effect of electric field intensity on the enhancement ratio r_{CHF} .

This study further analyzes why the numerical results are larger than the predicted values at high electric field intensity. The CHF correlation (i.e., Eq. (14)) given by Johnson et al.^[30] was obtained based on the assumption that the electrical force acts uniformly at the vapor-liquid interface (i.e., the electric field reduces only the Taylor wavelength). The above assumptions are reasonable for uniform electric fields on smooth surfaces, but some limitations are identified for non-uniform electric fields on surfaces with microstructures. Figure 14 demonstrates the interface evolution of the heating surface in the CHF state at different electric field intensities. When the electric field intensity $E_0=0$, the microcavity is covered by a stable vapor film. As the electric field intensity increases ($0 < E_0 \leq 0.065$), the vapor film in the microcavity shows intermittent breakup and regeneration under the perturbation of the electrical force, which indicates that the electric field enhances the CHF by decreasing the Taylor wavelength. When the electric field intensity was sufficiently large ($E_0=0.080$), pinning was produced at the position of the contact line at the junction of the conducting and insulating surfaces. The development of capillary waves in the microcavity was suppressed because of the non-uniform distribution of the electrical force. This phenomenon leads to the reflux of the bulk liquid and the formation of vapor jets to become well-ordered, significantly increasing the CHF. Thus, the modified correlation equation underestimates the enhancement ratio r_{CHF} when the electric field intensity is sufficiently large (Fig. 13).

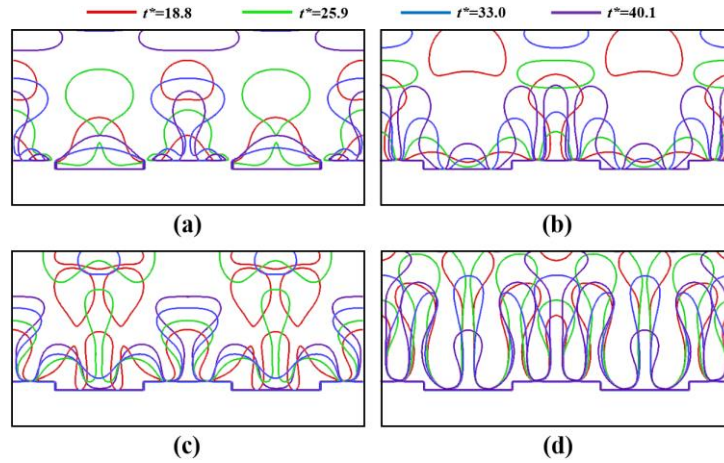


Fig. 14 The interfacial evolution of the heating surface in the CHF state. (a) $E_0 = 0$, (b) $E_0 = 0.050$, (c) $E_0 = 0.065$, (d) $E_0 = 0.080$.

5. Conclusions

In this study, lattice Boltzmann simulations find that coupled electric fields and microcavities with conducting-insulating surfaces can enhance boiling heat transfer synergistically. When the microcavity corners are insulated, the electrical forces can be reorganized, which improves the bubble formation process. The heating surface's boiling characteristics and heat transfer mechanism were analyzed under different superheat and electric field intensities. The main conclusions are as follows:

- (1) Microcavity surfaces may produce lower CHF than smooth surfaces. When the two-phase flow density ratio is lower, the bubbles produced at the bottom of the microcavity are larger and tend to merge to form a vapor film, hindering the bulk liquid's reflux and thus resulting in a lower CHF.
- (2) Conducting-insulating surfaces under the action of the electric field can eliminate the field trap effect caused by the microcavity structure. After insulating the corner structure, the bottom and the top of the microcavity generate a large electrical force, rapidly pushing the bubbles out of the heating surface and avoiding the mutual merging of the bubbles at medium superheat.
- (3) The electrical force can achieve CHF enhancement by destabilizing the vapor layer. When the electric field intensity is low, intermittent breakup and regeneration of the vapor film in the microcavity occurs under the perturbation of the electrical force. When the electric field intensity is large, the electrical force pins the contact line at the junction of the conducting and insulating surfaces. Thus, it facilitates the formation of a stable vapor-liquid separation path, improving the boiling heat transfer performance in the cavity and significantly enhancing the CHF.

Acknowledgements

The authors are grateful for the support of the National Natural Science Foundation of China (Grant Nos. 11872083 and 12172017).

Date Availability

The data that support the findings of this study are available from the corresponding author upon reasonable request.

References

- [1] I. Mudawar, Assessment of high-heat-flux thermal management schemes, *IEEE transactions on components and packaging technologies* 24 (2001) 122-141.
- [2] A. Mehrizadeh, S. R. Shabaniyan, G. Bakeri, Effect of modified surfaces on bubble dynamics and pool boiling heat transfer enhancement: A review, *Thermal Science and Engineering Progress* 15 (2020) 100451.
- [3] Q. Li, J. Zhao, X. Sun, B. Liu, Experimental investigation of pool boiling heat transfer on pillar-structured surfaces with different wettability patterns, *Applied Thermal Engineering* 215 (2022) 118924.
- [4] Y. Park, H. Kim, J. Kim, H. Kim, Measurement of liquid–vapor phase distribution on nano- and microstructured heating surfaces, *International Journal of Multiphase Flow* 81 (2016) 67-76.
- [5] X. Wang, J. Xu, H. Jiang, Y. Liu, X. Li, D. Shan, B. Guo, Achieving robust and enhanced pool boiling heat transfer using micro–nano multiscale structures, *Applied Thermal Engineering* 227 (2023) 120441.
- [6] Y. Kang, G. Wu, Z. Lang, H. Zhao, An experimental and numerical study of pool boiling heat transfer in Cu foam-enhanced cells with interlaced microchannels, *Applied Thermal Engineering* 225 (2023) 120158.
- [7] S. H. Kim, G. C. Lee, J. Y. Kang, K. Moriyama, M. H. Kim, H. S. Park, Boiling heat transfer and critical heat flux evaluation of the pool boiling on micro structured surface, *International Journal of Heat and Mass Transfer* 91 (2015) 1140-1147.
- [8] M. M. Rahman, E. Olceroglu, M. McCarthy, Role of wickability on the critical heat flux of structured superhydrophilic surfaces, *Langmuir* 30 (2014) 11225-11234.
- [9] J. Zhou, Y. Zhang, J. Wei, A modified bubble dynamics model for predicting bubble departure diameter on micro-pin-finned surfaces under microgravity, *Applied Thermal Engineering* 132 (2018) 450-462.
- [10] A. Inbaoli, C. S. S. Kumar, S. Jayaraj, A review on techniques to alter the bubble dynamics in pool boiling, *Applied Thermal Engineering* 214 (2022) 118805.
- [11] P. Wang, P. L. Lewin, D. J. Swaffield, G. Chen, Electric field effects on boiling heat transfer of liquid nitrogen, *Cryogenics* 49 (2009) 379-389.
- [12] S. A. Zonouzi, H. Aminfar, M. Mohammadpourfard, A review on effects of magnetic fields and electric fields on boiling heat transfer and CHF, *Applied Thermal Engineering* 151 (2019) 11-25.
- [13] P. Di Marco, W. Grassi, G. Memoli, T. Takamasa, A. Tomiyama, S. Hosokawa, Influence of electric field on single gas-bubble growth and detachment in microgravity, *International Journal of Multiphase Flow* 29 (2003) 559-578.
- [14] A. I. Garivalis, G. Manfredini, G. Saccone, P. D. Marco, A. Kossolapov, M. Bucci, Critical heat flux enhancement in microgravity conditions coupling microstructured surfaces and electrostatic field, *npj Microgravity* 7 (2021) 37.
- [15] X. Quan, M. Gao, P. Cheng, J. Li, An experimental investigation of pool boiling heat transfer on smooth/rib surfaces under an electric field, *International Journal of Heat and Mass Transfer* 85 (2015) 595-608.
- [16] B. Liu, A. I. Garivalis, Z. Cao, Y. Zhang, J. Jia, P. D.marco, Effects of electric field on pool boiling heat transfer over microstructured surfaces under different liquid subcoolings,

- International Journal of Heat and Mass Transfer 183 (2022) 122154.
- [17] W. Li, Q. Li, H. Chang, Y. Yu, S. Tang, Electric field enhancement of pool boiling of dielectric fluids on pillar-structured surfaces: A lattice Boltzmann study, *Physics of Fluids* 34 (2022) 12.
- [18] H. Chang, B. Liu, Q. Li, X. Yang, P. Zhou, Effects of electric field on pool boiling heat transfer over composite microstructured surfaces with microcavities on micro-pin-fins, *International Journal of Heat and Mass Transfer* 205 (2023) 123893.
- [19] Q. Li, K. H. Luo, X. J. Li, Lattice Boltzmann modeling of multiphase flows at large density ratio with an improved pseudopotential model, *Physical Review E* 87 (2013) 053301.
- [20] Q. Li, Q. J. Kang, M. M. Francois, Y. L. He, K. H. Luo, Lattice Boltzmann modeling of boiling heat transfer: The boiling curve and the effects of wettability, *International Journal of Heat and Mass Transfer* 85 (2015) 787-796.
- [21] S. Gong, P. Cheng, Lattice Boltzmann simulation of periodic bubble nucleation, growth and departure from a heated surface in pool boiling, *International Journal of Heat and Mass Transfer* 64 (2013) 122-132.
- [22] Y. Feng, H. Li, K. Guo, X. Lei, J. Zhao, Numerical study on saturated pool boiling heat transfer in presence of a uniform electric field using lattice Boltzmann method, *International Journal of Heat and Mass Transfer* 135 (2019) 885-896.
- [23] W. M. Rohsenow, A method of correlating heat-transfer data for surface boiling of liquids, *Transactions of the American Society of Mechanical Engineers* 74 (1952) 969-975.
- [24] N. Zuber, Hydrodynamic aspects of boiling heat transfer (thesis), Ramo-Wooldridge Corp., Los Angeles, CA (United States); Univ. of California, Los Angeles, CA (United States) (1959).
- [25] G. Liang, I. Mudawar, Pool boiling critical heat flux (CHF)–Part 1: Review of mechanisms, models, and correlations, *International Journal of Heat and Mass Transfer* 117 (2018) 1352-1367.
- [26] R. S. Allan, S. G. Mason, Particle behaviour in shear and electric fields I. Deformation and burst of fluid drops, *Proceedings of the Royal Society of London. Series A. Mathematical and Physical Sciences* 267 (1962) 45-61.
- [27] F. Cai, Z. Liu, N. Zheng, Y. Ren, Y. Pang, Lattice Boltzmann simulation of the effects of cavity structures and heater thermal conductivity on nucleate boiling heat transfer, *Applied Mathematics and Mechanics* 44 (2023) 981-996.
- [28] A. M. Gheithaghy, A. Samimi, H. Saffari, Surface structuring with inclined minichannels for pool boiling improvement, *Applied Thermal Engineering* 126 (2017) 892-902.
- [29] B. P. Benam, V. E. Ahmadi, A. R. Motezakker, S. Saeidiharzand, L. G. Villanueva, H. S. Park, A. K. Sadaghiani, A. Koşar, A parametric study on pool boiling heat transfer and critical heat flux on structured surfaces with artificial cavities, *Applied Thermal Engineering* 221 (2023) 119841.
- [30] R. L. Johnson, Effect of an electric field on boiling heat transfer, *AIAA journal* 6 (1968) 1456-1460.
- [31] S. W. J. Welch, G. Biswas, Direct simulation of film boiling including electrohydrodynamic forces, *Physics of fluids* 19 (2007).
- [32] S. Gong, L. Zhang, P. Cheng, E. N. Wang, Understanding triggering mechanisms for critical heat flux in pool boiling based on direct numerical simulations, *International Journal of Heat and Mass Transfer* 163 (2020) 120546.